Design and manufacturing a small-scale radial-inflow turbine for clean organic Rankine power system

Al Jubori, Ayad M.; Al-Mousawi, Fadhel N.; Rahbar, Kiyarash; Al-Dadah, Raya; Mahmoud, Saad

DOI:
10.1016/j.jclepro.2020.120488

Document Version
Peer reviewed version

Citation for published version (Harvard):
Al Jubori, AM, Al-Mousawi, FN, Rahbar, K, Al-Dadah, R & Mahmoud, S 2020, 'Design and manufacturing a small-scale radial-inflow turbine for clean organic Rankine power system', *Journal of Cleaner Production*, vol. 257, 120488, pp. 1-13. https://doi.org/10.1016/j.jclepro.2020.120488

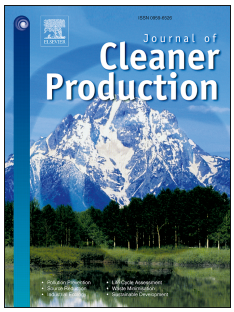

Design and manufacturing a small-scale radial-inflow turbine for clean organic Rankine power system

Ayad M. Al Jubori, Fadhel N. Al-Mousawi, Kiyarash Rahbar, Raya Al-Dadah, Saad Mahmoud

PII: S0959-6526(20)30535-7

DOI: https://doi.org/10.1016/j.jclepro.2020.120488

Reference: JCLP 120488

To appear in: *Journal of Cleaner Production*

Received Date: 12 July 2019

Revised Date: 22 January 2020

Accepted Date: 7 February 2020

Please cite this article as: Al Jubori AM, Al-Mousawi FN, Rahbar K, Al-Dadah R, Mahmoud S, Design and manufacturing a small-scale radial-inflow turbine for clean organic Rankine power system, *Journal of Cleaner Production* (2020), doi: https://doi.org/10.1016/j.jclepro.2020.120488.

Design and manufacturing a small-scale radial-inflow turbine for clean organic Rankine power system

Ayad M. Al Jubori [a,c*], Fadhel N. Al-Mousawi [b], Kiyarash Rahbar [c], Raya Al-Dadah [c], Saad Mahmoud [c]

[a] Communication Engineering Department, University of Technology – Iraq
[b] Department of Mechanical Engineering, University of Karbala, Karbala, Iraq
[c] School of Engineering, The University of Birmingham, Birmingham, UK
* Email: 11017@uotechnology.edu.iq ; ayadms@gmail.com

Abstract

With growing on the energy demand and availability of the low-grade temperature heat source, the organic Rankine cycle as a power system can be efficiently utilized to generate electricity. The turbine design and its performance have the main impact on determining the system power and overall system efficiency. Therefore, design a small-scale organic Rankine system requires the development of an appropriate turbine. To achieve this aim, this work offers an innovative complete design method to develop a radial-inflow turbine for small-scale organic Rankine cycle power applications, which includes a preliminary design (i.e. one-dimensional design calculation phase) and a three-dimensional flow analysis using the computational fluid dynamic technique. A thermodynamic analysis of the organic Rankine cycle was integrated with the design methodology. Where the three-dimensional geometry model was built based on the thermodynamic and aerodynamic design, and then was imported into the ANSYS-CFX software to conduct viscous numerical simulations. The optimum design of the radial-inflow turbine was manufactured using a three-dimensional printing (pioneering) technique, and the experimental testing was conducted at off-design points to validate the turbine design.

The evaluation of the turbine's performance (efficiency and power) was presented under design and off-design points in terms of rotational speeds, expansion ratios, and inlet temperatures with five different organic fluids. The turbine numerical results showed that R600 as a working fluid has a higher predicted turbine efficiency of 78.32% and power of 4.8 kW with cycle thermal efficiency of 9.15% compared with 8.045% for R245fa. Depending on the experimental results at off-design points, the highest cycle thermal efficiency of 4.25% with a turbine efficiency of 45.22% was achieved. These results assured the precision of the proposed PD methodology at off-design points in making performance maps of the turbine.

Keywords: Organic Rankine cycle; radial-inflow turbine; Preliminary design; 3D CFD simulations; Thermodynamic analysis; Organic fluids, Turbine manufacturing

1. Introduction

Recently, delivering sustainable energy systems is one of the key challenges faced by the society, where power production using fossil fuel resources is accompanied by emissions leading to environmental impacts such as local pollution, acid rain, geopolitical disorders, and global climate change. Moreover, the organic Rankine cycle (ORC) system has received more attention as a one waste heat recovery (WHR) system in low-to-medium grade heat source temperature compared with the conventional system (i.e. steam Rankine cycle). In the ORC system, the refrigerants/hydrocarbons (organic fluid) are used as alternative working fluids to conventional fluids i.e. water/steam because of the low-boiling temperature of the organic fluids.

The turbine is the most critical component through the ORC system, and it is a work/power-generating device. Therefore, the ORC turbines have received increasing interest in terms of design and analysis. Therefore, several studies have been carried out on the ORC system based on the radial-inflow turbine (RIT) using the one-dimensional preliminary design (PD) and three-dimensional simulation in terms of computational fluid dynamics (CFD) technique, as reported in Table 1.

Table 1 Review of the turbine design methodology

Authors	Research approach	Organic working fluids	Temperature of heat sources (K)	Performance (turbine, power output and efficiency, system efficiency)
Cho et al. (2014)	CFD investigation for stator	R245fa	393	3.8 kW, 53%, 6.25%
Costall et al. (2015)	Preliminary mean-line design (1D)	Toluene	640-840	45.6 kW, 56.1%
Li and Ren (2016)	1D, 3D design and simulation	R123	393	534 kW, 84.33%
Nithesh and Chatterjee (2016)	3D CFD study	R134a	297.5	2 kW, 70%%
Russell et al. (2016)	1D and 3D CFD analysis (rotor only)	R245fa	423	7 kW, 76%
Al Jubori et al. (2017b)	1D and 3D CFD analysis	R141b, R245fa, and isopentane	365	15.798 kW, 84.64%,, 13.96%
Kim and Kim (2017)	1D design and CFD simulation	R143a	413	400 kW, 79.56%
Stijepovic et al. (2017)	1D design and theodynamic analysis	Benzene, Pentafluor-opropan	678.15	1613.97 kW and system efficiency 14.27%
Zheng et al. (2017)	1D and 3D CFD analysis	R134a	360	643 kW, 81.6%
Lv et al. (2018)	1D design and CFD simulation	S-CO_2	943	85%

From the experimental side, Pei et al. (2011) experimentally studied the ORC system using RIT under varying conditions with R123 as a working fluid. Their results indicated that the highest ORC system efficiency of 6.8% and RIT efficiency of 65% were achieved at a maximum temperature difference of 70 °C between the heat source and heat sink. Moreover, the mass flow rate through the turbine was unequal to that through the pump. Li et al. (2015) conducted an experimental analysis on the performance of the scroll expander for the ORC system with R245fa and R245fa/R601a as the working fluids. They exhibited that the system thermal efficiency with R345fa was 4.38% compared with 4.45% for R245fa/R601a at the design expansion ratio. Moreover, their results indicated that the working charge has an impact on the ORC system performance. Shao et al. (2017) investigated by experiments a micro RIT for ORC system using R123 as a working fluid. The performance characteristic in terms of electric power of 1.884 kW was achieved when the rotational speed of 34586 rpm was reached. They found that the performance for both the turbine and the system was increased with the temperature of the heat source. Alshammari et al. (2018) experimentally assessed a small ORC system as a waste heat recovery system based on RIT turbine with R1233zde as a working fluid. The developed system was utilized in a heavy-duty diesel engine application, and tested under a partial load with the rotational speed at the design point. They achieved a maximum thermal efficiency of 4.3% and a turbine efficiency of 35% at a rotational speed of 20000 rpm. Weiß et al. (2018) conducted an experimental study of the ORC system performance and behaviour depending on the micro impulse turbine and radial cantilever. The measured turbine power output of 12 kW and efficiency of 76.8% was attained with Hexamethyldisiloxane as a working fluid at pressure ratio 22.4 and rotational speed of 27000 rpm. Furthermore, the throttle should be replaced by the turbine in the low-temperature cycle.

In order to enhance the ORC system performance, Kang (2016) performed an experimental study of the RIT in a two-stage shape using R245fa at an evaporator temperature of 116 °C and a pressure ratio of 11.6. The preliminary tests were carried out to examine the designed ORC system performance characteristics. They found that the ORC system efficiency of 9.8%, with a turbine efficiency of 68.5% and a power output of 39.0 kW. Sung et al. (2016) experimentally investigated the performance of a two-stages RIT for the ORC system. The experiments were conducted at the design point in terms of the mass flow rate of 7.2 kg/s, evaporator pressure of 20.90 bars, and the evaporator temperature of 413 K with R245fa as a working fluid. Their experimental results showed that the maximum turbine efficiency of 68.1%, net power of 177.4 kW, and system efficiency of 9.6% were achieved compared with a net power of 165 kW at a partial load. Chen et al. (2019) carried out a theoretical and experimental

study on double-stage RIT turbine performance for a 15 kW ORC system driven by ocean thermal energy. R717 was used as a working fluid. They found that the maximum ORC system efficiency of 1.9543% at an inlet pressure of 1.5 MPa was achieved based on the experimental test.

In terms of the volumetric expander, Yang et al. (2018) conducted an experimental analysis of the scroll expander for a small-scale ORC system. R1233zd(E) was used as the alternative organic working fluid for R245fa. They found that R1233zd(E) has a better cycle thermal efficiency of 3.76% compared to 3.62% for R245fa with a mass flow rate of 160 kg/h and a rotational speed of 1550 rpm. Ziviani et al. (2018) tested the scroll expander which was integrated with an ORC system of 5 kW scale with the working fluid R245fa. The system was investigated under a low-temperature heat source of 65°C and 110°C respectively, and the rotational speeds ranged between 800 rpm and 3000 rpm. They found the maximum expander efficiency to be 56% at the internal volume ratio of 6.55. Xi et al. (2019) carried out an experimental study on a simple and regenerative ORC system using the scroll expander with the working fluid R123. Comparison with two suction volumes of 66 mL/r and 86 mL/r was conducted. They exhibited that the maximum measured system efficiency was 2.96% with a suction volume of 86 mL/r.

Particularly in low-grade heat source temperature, the temperatures are often unstable and non-controlling. Consequently, it is very important to explore the turbine's performance under various operating conditions. Although several studies have been done on the ORC system based on an RIT turbine, only limited experimental works have carried out to investigate the performance of a small scale RIT turbine. Most of the ORC system based on the RIT driven by the low-temperature heat sources were either theoretical investigations or experimental studies based on prototypes. Where there is no sufficient information on how to design and manufacture these prototypes.

In the current study, the performance of the RIT turbine is numerically and experimentally explored at design and off-design conditions, and the influences of the heat source temperatures, expansion ratios, and rotational speeds on the turbine performance are clarified. Moreover, the impacts of working fluids on RIT performance are also presented. Depending on the authors' knowledge, the literature quiet lacks of such models for a small scale radial inflow turbine for ORC system application. The current work aims to develop a new systematic prediction methodology of a small-scale RIT turbine for the ORC system based on the PD method with a genetic optimization algorithm, 3D CFD simulations, ORC thermodynamic system analysis, and manufacturing of RIT based on 3D printing technique, and experimental tests for validation purposes.

2. Organic Rankine cycle modelling

The simple configuration of the sub-critical ORC system, displayed in Fig. 1a, is appropriate for organic fluids with a positive slope (dT/ds) of the saturation vapour curve of the working fluid on the T-s diagram (Temperature-entropy diagram). Where, the working fluid vapour at the turbine outlet is superheated, as shown in Fig. 1b. Here, the sub-critical ORC system is considered and investigated under steady-state conditions, neglecting heat losses and pressure drop. Table **2** presents the operating conditions that were applied in the ORC system modelling. Engineering equation software (EES) (Klein, 2013) was used to model the ORC system. More details about the ORC system modelling can be found in the previous studies as Al Jubori et al. (2016) and Al Jubori et al. (2017a).

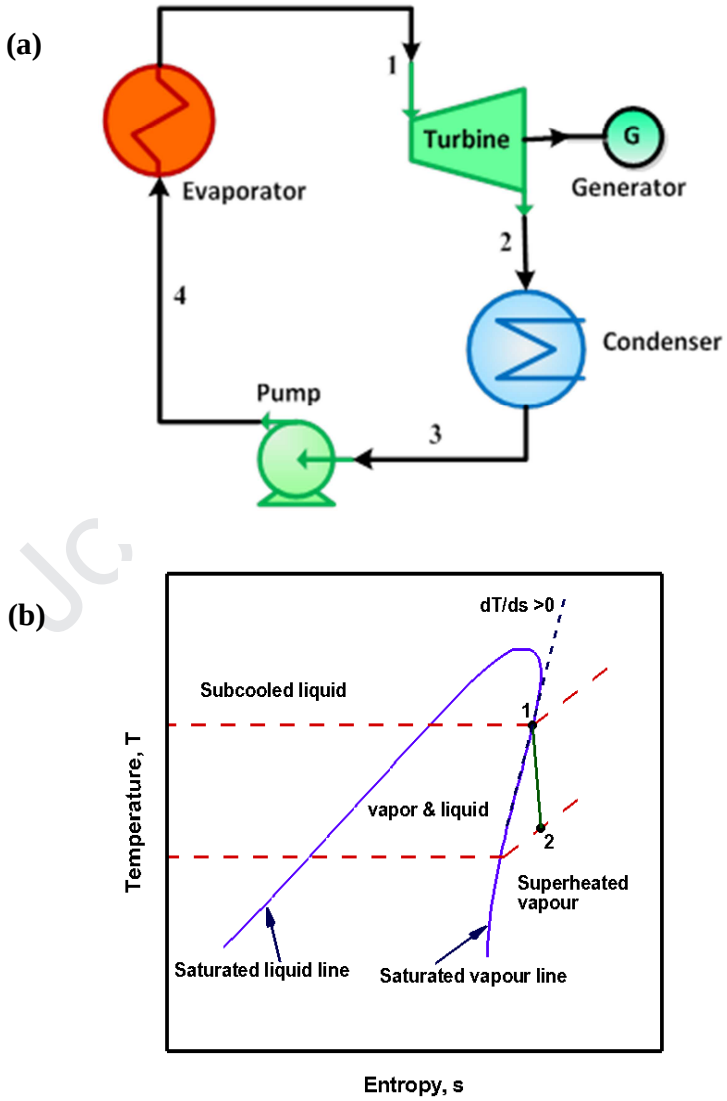

Fig. 1 Simple sub-critical ORC system configuration (a), T-s graph for dry (positive slope) working fluid (b)

Table 2 input and operating conditions of the organic Rankine cycle and turbine design

Parameters	Values/Ranges	Unit
Working fluid temperature at turbine inlet	340-365	K
Working fluid pressure at turbine inlet	[a]	bar
Superheating degree of working fluid	0-5	K
Expansion ratio	1.5-4 [b]	-
Condensing pressure	Equivalent saturated pressure at cold source temperature	bar
Heat sink temperature	298	K
Mass flow rate of working fluids	0.25	kg/s
Mechanical efficiency	0.96	
Generator efficiency	0.96	-
Pump efficiency	0.75	-
Reaction (R_n)	0.4-0.6	-
Loading coefficient (Ψ)	0.8-0.9	-
Flow coefficient (ϕ)	0.2-0.3	-
Rotational speed	10000-50000	rpm
Blade speed ratio	0.7	-
Rotor RIT exit absolute flow angle (α_5)	0	degree
Velocity ratio at meridional of the rotor (ξ)	0.5-0.8	-
Working fluids	R141b, R245fa, R600, HFE7000 and isopentane	-

[a] Matching saturated vapour pressure at inlet temperature
[b] Corresponding to the condenser pressure

3. Radial-inflow turbine design methodology

3.1. Preliminary design (PD) of RIT turbine

Fig. 2a presents three parts, namely stator, rotor, and volute, that make up the RIT stage. Fig. 2b displays the rotor blade profile of the RIT stage with a velocity triangle. The PD methodology outlined in (Moustapha et al., 2003; Whitfield and Baines, 1990) was applied to develop the RIT, where two non-dimensional parameters (i.e. loading and flow coefficients) were employed to get the preliminary turbine efficiency. The development PD methodology involved a genetic algorithm optimization technique that is integrated with the PD model to assess the influence of the design input parameters on the turbine performance and geometry. Moreover, there are two additional dimensionless variables, specific speed, and specific diameter, which are utilised to provide the initial RIT performance. Specific speed (N_s) is the ratio between the volumetric flow rate and the ideal work, and it can be calculated as follows:

$$N_s = \frac{\Omega \sqrt{\frac{\dot{m}}{\rho_{exit}}}}{(\Delta h_{is})^{0.75}} \quad (1)$$

Specific diameter (D_s) refers to the size of the turbine in terms of dimensionless variable, which is calculated as below:

$$D_s = \frac{d_{rotor}\,(\Delta h_{is})^{0.25}}{\sqrt{\frac{\dot{m}}{\rho_{exit}}}} \quad (2)$$

In the preliminary design of the RIT, the performance was presented in terms of enthalpy losses which comprise incidence, tip clearance, windage, secondary losses, friction loss, stator, and volute, as enumerated in Table 3. The RIT performance (i.e. efficiency) was determined depending on the obtained losses of the RIT stage and utilised as the preliminary estimated value of the following generation of iteration technique. The turbine losses model was validated against a gas turbine using air and an ORC turbo-expander using R245fa at the operating condition close to the design condition. The input parameters, as shown in Table **2**, were applied to the RIT preliminary design. Engineering equation software (EES) (Klein, 2013) was utilized to implement the preliminary design code of the RIT. The RIT isentropic efficiency in terms of total-to-total efficiencies are obtained based on Ventura et al. (2012) as follows:

$$\eta = \frac{\Delta h_{actual}}{\Delta h_{actual} + \sum(\Delta h_{total\ losses})} \quad (3)$$

The total losses in terms of enthalpy drop can be obtained as following:

$$\sum(\Delta h_{total\ losses})_{total-to-total} = \Delta h_{incidence} + \Delta h_{secondary} + \Delta h_{friction} + \Delta h_{tip\ clearance} + \Delta h_{windage} + \Delta h_{Stator,friction} + \Delta h_{Volute,loss} \quad (4)$$

$$\eta_{tt} = \frac{h_{01} - h_{05}}{h_{01} - h_{05ss}} = \frac{h_{01} - h_{05}}{h_{01} - h_{05} + \sum(\Delta h_{total\ losses})_{total-to-total}} \quad (5)$$

where, h_{01} and h_{05} represent the total enthalpy at inlet and outlet of the turbine stage respectively, and h_{05ss} represents the isentropic total enthalpy at the stage exit.

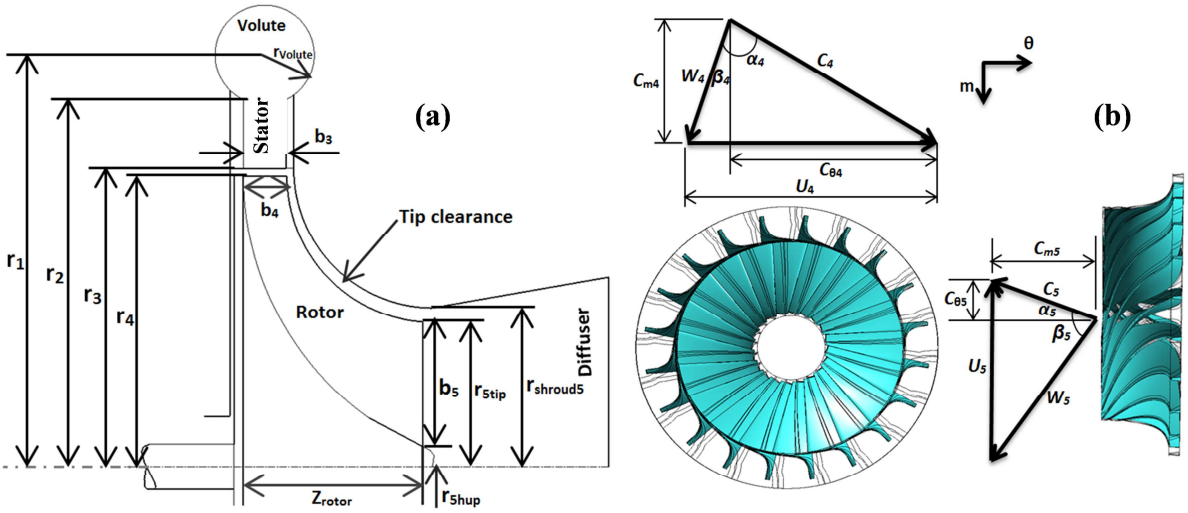

Fig. 2 Schematic of radial-inflow stage (a); rotor blades and velocity triangles (b)

144

145 Table 3 Turbine losses model

Category of losses	Correlations	References
Incidence loss	$\Delta h_{incidence} = \frac{w_{\theta 4}^2}{2}$	Ventura et al. (2012)
Tip clearance loss	$\Delta h_{tip\ clerance} = \frac{U_4^3 . Z_{rotor}}{8\pi}\left(0.4.\varepsilon_x.C_x + 0.75.\varepsilon_r.C_r - 0.3\sqrt{\varepsilon_x.\varepsilon_r.C_x.C_r}\right)$	Moustapha et al. (2003)
Secondary loss	$\Delta h_{secondary} = \frac{C_4^2 . d_4}{Z_{rotor}.r_c}$	Moustapha et al. (2003)
Friction loss	$\Delta h_{friction} = f_{curve}\left[\frac{w_4 + \left(\frac{w_{5tip} + w_{5hub}}{2}\right)}{2}\right]\frac{l_{hyd}}{d_{hyd}}$	Ventura et al. (2012)
Windage loss	$\Delta h_{windage} = k_f \frac{\bar{\rho}.U_4^3 r_4^2}{2.\dot{m}.w_5^2}$	Moustapha et al. (2003)
Nozzle friction loss	$\Delta h_{friction} = 4.f_{nozzle}.\bar{C}\frac{l_{hyd}}{d_{hyd}}$	Ventura et al. (2012) , Moustapha et al. (2003)
Volute loss	$\Delta h_{volute\ loss} = \frac{K_{volute} C_2^2}{2}$	Whitfield and Baines (1990)

146

147 **3.2. 3D Radial-inflow blade module**

148 The preliminary stage geometry of the RIT (i.e. stator and rotor) from the PD code were transferred into the Blade-
149 Gen module in ANSYS®18.2 workbench to create the profile of the rotor and stator blades in three-dimensional form.
150 The thickness distribution model was applied to generate the rotor blades. The CFD analysis is used in order to
151 deliver more accurate and efficient RIT turbine geometry leading to more realistic aerodynamics' characteristics and

performance by capturing the 3D flow features. The performance of the RIT turbine can be improved depending on the parametric studies, in terms of the blade geometry design parameters. Therefore, to obtain the optimum 3D configuration of the blade geometry it is necessary to investigate various blade configurations based on blade and flow angles, number of blades, blade pitch…etc. Moreover, the evaluation of the aerodynamic characteristic and performance of the RIT turbine requires creating the blade geometry and modifying it and testing it using CFD simulation in more detail. More details about the blade generation of RIT can be found in Al Jubori et al. (2017b).

3.3. Mesh generation

To highly automate the meshing of the RIT blade passages, the TurboGrid technique in ANSYS®18.2 workbench was used, which is based on a hexahedral mesh that is constructed in the shape of an O-H grid. An independent study of the grid generation was carried out to obtain the number of mesh nodes that were deemed essential for an accurate solution. The computational grid was clustered, the solution re-ran and the procedure repeated until the simulation was independent of the grid number where the simulation was found to be mesh-independent above 615,000 and 490,000 nodes for the rotor and stator, respectively.

3.4. CFD analysis

The governing equations including the RANS equations (i.e. Reynolds-averaged Navier–Stokes equations) with shear stress transport (SST)/k-ω turbulence model equations have been solved based on the high-resolution advection scheme (HRAS). The turbulence closure was captured using an automatic wall-function that depended on the definition of y^+ (dimensionless distance) the node's wall (i.e. first node after the wall) at a value of $\leq$1, as suggested in (ANSYS CFX-Solver Modelling Guide, 2017). All RIT stage walls were fixed in the CFX set-up as non-slip, smooth and adiabatic. For all simulations, the CFD solution was obtained at the convergence of a maximum RMS value $\leq$ 1e-5 for the calculated parameters, namely: mass, momentum, turbulence model and energy.

To consider the changes in the working fluid properties (i.e. organic fluid), an accurate thermodynamic model of the ORC turbine is required to achieve the three-dimensional simulation using the computational fluid dynamics technique to capture the variations in the working fluid properties and the flow characteristic over the expansion process through the RIT stage. One of the most accurate two-parameter equations of state is the Redlich-Kwong equation of state according to (ANSYS CFX-Solver Modelling Guide, 2017). Obtaining more precise results from

the Redlich-Kwong equation of state at a critical point, Aungier modified it to call then Aungier Redlich Kwong. Therefore, the Redlich-Kwong equation of state was developed to overcome the limitations in predicting liquid properties and vapour-liquid equilibrium near a critical point. Moreover, the REFPROP software database of the real organic fluids properties was combined with the ANSYS®18.2-CFX for better predictability of the working fluids' behaviour through the turbine stage (Lemmon et al., 2007).

3.5. Experimental facility

The schematic drawing of the developed ORC test rig is displayed in Fig. 3, which has been constructed to assess the ORC system based on the RIT turbine. The ORC test facilities comprise an evaporator, a condenser, an RIT, a refrigerant pump, water and vacuum pumps, a control system and instrumentation. Moreover, a water electrical heater was connected beside the cold and hot water tanks to function as the heat and sink sources, respectively. The transducers of the total pressure, temperature sensors, refrigerant flow meter, and torque meter were utilised to calculate power output and efficiencies of the RIT and ORC systems. The RIT turbine for the working fluid R245fa was manufactured depending on the mean-line design and the CFD simulations, where three-dimensional printing tools were employed. R245fa as a working fluid is a safe refrigerant in terms of non-toxic, non-flammable. R600 is classified as highly flammable as its main drawback and its flammability should attract enough attention. From the perspectives of environmental, safety aspects and its availability in our laboratory, R245fa was used in the current experimental work.

Fast prototyping based on 3-D printing i.e. additive layer manufacturing technique can be considered as a growing technology with significant evolutions in the last decade. The final design of the modules of the RIT turbine were manufactured using 3D printing technique based on additive layer and CNC (computer numerical control) machines. The low-carbon steel powder was used in manufacturing. The standard inkjet printing technology was utilized in the 3D printing machines through making the portions layer-by-layer by putting a liquid binder onto the powder thin layers. As shown in Fig. 4, the main parts of the RIT turbine, include the stator, rotor and volute. The volute guides the working fluid to the stator with minimum loss.

The working fluid through the volute is in a superheated/saturated vapour state and then enters the blade passages of the stator in the radial direction. The working fluid through the stator blades passages passes into the rotor which, in turn, is connected to the shaft to measure the torque, rotational speed using the torque meter. In addition, the bearing housing and rotor shaft were assembled with the housing of the shaft seal to stop the leakage of the working fluid

208 through the interaction region between the bearing and the shaft. The evaporator outlet was connected with the RIT
209 turbine inlet while its outlet to the inlet of the condenser. The measuring devices were installed across the ORC
210 system to record and calculate the working fluid properties. Commissioning was commenced after completing the
211 installation of all components of the ORC system and pipe networks with valves and instrumentations to ensure that
212 the ORC system works safely at the range of testing conditions.
213 The state of the working fluid (i.e. R245fa) at the inlet and outlet of the main ORC system components was
214 determined using the measurements of both pressure and temperature. Moreover, the state of the working fluid as
215 superheated vapour was guaranteed based on the measured data (pressure and temperature). Depend on the
216 measured data namely: the temperature and pressure of the working fluid vapour, torque, rotational speed, working
217 fluid mass flow rate, the RIT turbine efficiency was calculated as:

$$\eta_{turbine} = \frac{\text{Power output}}{\dot{m}(\Delta h_{isentropic})} = \frac{\dot{W}_t}{\dot{m}(\Delta h_{isentropic})} \quad (6)$$

218 where $\Delta h_{isentropic}$ is the ideal enthalpy difference at the inlet and outlet of the RIT turbine through the isentropic
219 expansion process when its entropy is the same as that at the inlet of the turbine. Where the specific enthalpy and
220 entropy at the turbine inlet are obtained in terms of the inlet temperature and pressure of the working fluid vapour.
221 The turbine power output was obtained in terms of the measured rotational speed (ω) and torque as following:

$$\dot{W}_t = \omega * Torque \quad (7)$$

222 where, ω is the rotational speed in (rad/s).
223

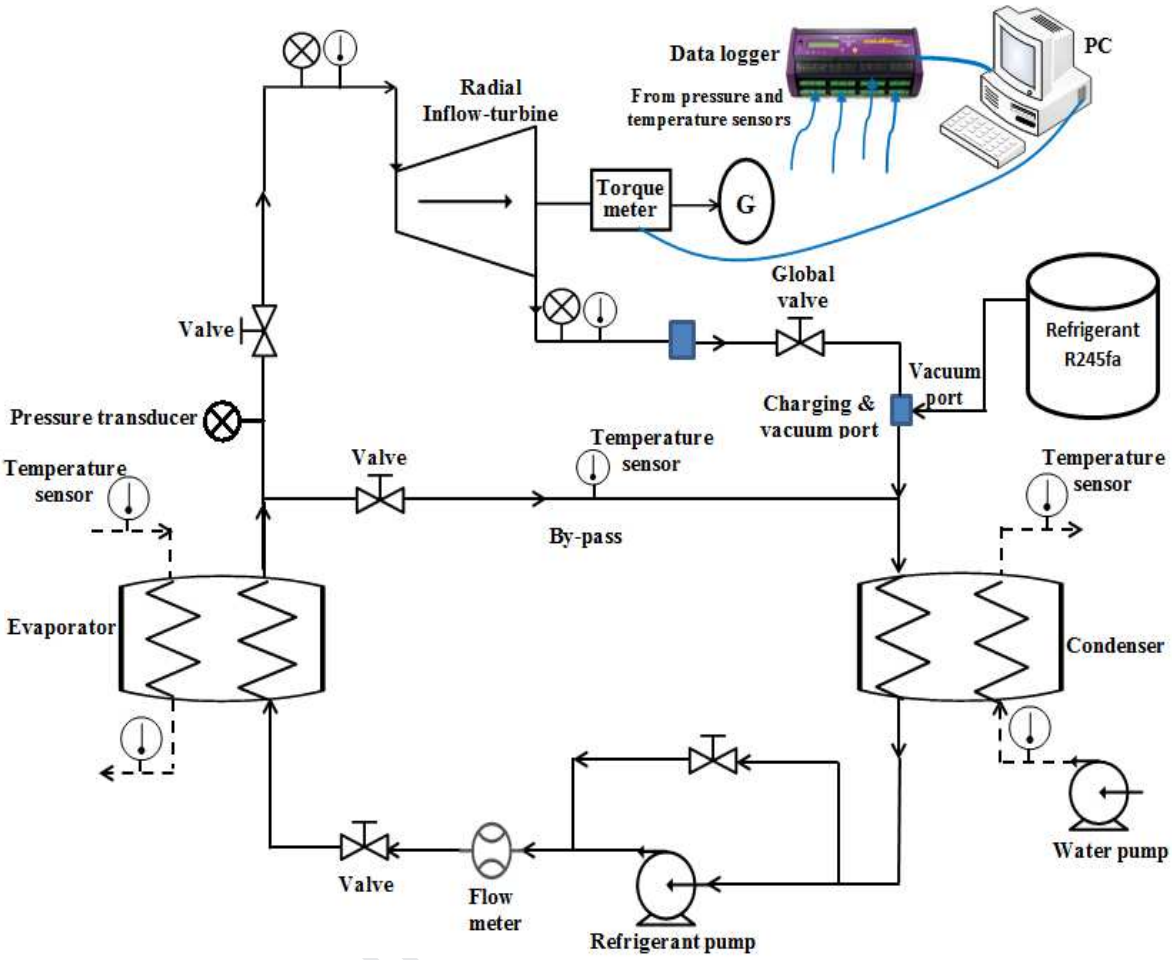

Fig. 3 Schematic drawing of the structured ORC system

224

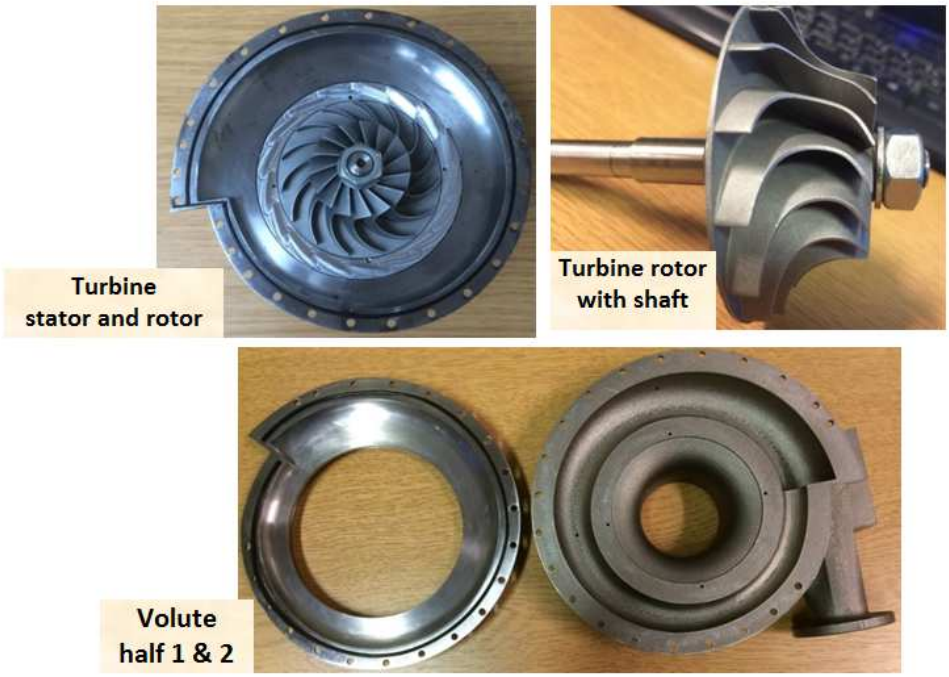

Fig. 4 Manufactured RIT stage in pictorial view

225

226 **3.5.1. Uncertainty analysis**

227 The measured parameters in terms of pressure, temperature, torque, and mass flow rate have some uncertainty thus
228 the calculations that include these parameters will have uncertainty. Consequently, for the experimental results in
229 terms of turbine efficiency and power, the EES code was employed to implement the uncertainty propagation using
230 the Root Sum Square (RSS) approach. In the RSS approach, the measured parameters are typically distributed
231 uncorrelated values. When the calculated parameter (Y) is a function of k readings (x_1 to x_k), then its individual
232 uncertainty can be expressed as ζ_{x_1} to ζ_{x_k}. Where the uncertainty in $Y(\zeta_y)$ can be presented in terms of measured
233 quantities as follows:

$$Y = f(x_1, x_2, x_3, \dots, x_k) \tag{8}$$

$$\zeta_{Y,x_i} = \frac{\partial Y}{\partial x_i}\,\zeta_{x_i} \tag{9}$$

234 The total uncertainty in Y in terms of the essential uncertainties are combined in the following equation:

$$\zeta_y = \sqrt{\left(\frac{\delta Y}{\delta x_1}\delta_{x_1}\right)^2 + \left(\frac{\delta Y}{\delta x_2}\delta_{x_2}\right)^2 + \cdots + \left(\frac{\delta Y}{\delta x_k}\delta_{x_k}\right)^2} \tag{10}$$

235 The overall accuracy for any measuring device involves systematic (bias) error and random (precision) error as
236 below:

$$\zeta_{overall} = \mp\sqrt{\zeta_{random}^2 + \zeta_{systematic}^2} \quad (11)$$

237 The random errors are calculated using the mean standard deviation with 95% confidence interval as follows:

$$\zeta_{random} = t_{N-1.95\%} S_{\bar{x}} \quad (12)$$

238 where, $t_{N-1.95\%}$ represents the student distribution number factor, N represents the number of readings, and the $S_{\bar{x}}$
239 represents the standard deviation which can be calculated as following:

$$S_{\bar{x}} = \frac{1}{\sqrt{N}}\sqrt{\frac{\sum_{i=1}^{N}(X_i - \bar{X})^2}{N-1}} \quad (13)$$

240 The systematic errors comprise the data acquisition error, the calibration errors and hysteresis errors were obtained
241 using the following equation:

$$\zeta_{systematic} = \sqrt{\sum_{i=1}^{M} \delta_{i,systematic}^2} \quad (14)$$

242 where, M represents the sources number of the systematic errors. It depends on the calibration errors and the
243 manufacturer.

244 **4. Results and discussion**

245 **4.1. CFD Results**

246 The main geometry dimensions and design parameters form the PD design, shown in Table 4, have been utilized to
247 generate the three-dimensional configuration of the RIT turbine model by ANSYS-CFX. The design operating
248 conditions comprised a mass flow rate of 0.25 kg/s, an expansion ratio of 3.0 and a turbine inlet temperature of 365
249 K with a rotational speed of 25,000 rpm for R600 and isopentane, 30,000 rpm for R141b, 35,000 rpm for R45fa and
250 40,000 for HFE7000.
251
252
253
254

Table 4 The delivered output from the RIT PD code for each considered working fluid

Parameter	R141b	R245fa	R600	HFE7000	Isopentane
d_1 (mm)	56.82	50.91	60.93	46.48	58.10
d_2 (mm)	46.87	43.38	52.16	38.87	50.05
d_3 (mm)	36.94	34.30	41.04	30.72	38.74
d_4 (mm)	33.15	31.28	37.15	26.21	35.12
$d_{tip,5}$ (mm)	25.46	23.13	28.62	20.17	26.29
b_4 (mm)	2.49	2.14	2.75	2.06	2.57
b_5 (mm)	18.87	17.402	22.19	15.22	20.67
β_4	37.74	11.69	40.56	10.29	38.57
$\beta_{blade,4}$	57.76	31.70	60.76	26.18	58.61
$\beta_{tip,5}$	-68.72	-61.69	-70.47	-51.31	-69.65
α_4	74.56	69.70	75.83	67.83	73.83
Degree of reaction (-)	0.530	0.520	0.535	0.511	0.531
Loading coefficient (-)	0.847	0.855	0.853	0.859	0.853
Flow coefficient (-)	0.263	0.257	0.271	0.252	0.268
Rotor blade number	15	13	15	11	15
Turbine Power (kW)	4.605	4.455	4.974	4.109	4.805
Turbine efficiency %	78.62	77.84	81.16	76.97	79.92

Fig. 5 and Fig. 6 depict the operational behaviour of the designed five different RIT for five different fluids. Fig. 6 presents the performance variations in RIT performance (i.e. power and efficiency) with rotational speed where it shows that with increased rotation speed, the turbine power and efficiency increase considerably to reach the optimum value at the desired point of the rotational speed and then decrease upon further increase after the design point. The maximum RIT power output and efficiency were found to be 4.80 kW and 78.32%, respectively, with the working fluid R600 at a rotational speed of 25,000 rpm compared to 74.69% and 4.447 kW for HFE7000 at the rotational speed of 40,000 rpm. This trend shows that the rotational speed at the design condition leads to high turbine efficiency and turbine power with five organic fluids. For the equal mass flow rate of the organic working fluid, a high-density organic fluid such as HFE7000 has the lowest diameter (i.e. size/volume) because of its smaller specific volumes and thus leads to an upper rotational speed based on the definition of the blade velocity. Moreover, lighter working fluid like R600 is able to generate a greater output power related to high-density organic fluids because of comparatively bigger rotor diameter. Therefore, higher enthalpy drop in terms of specific work output can be achieved with lighter working fluid (i.e. light molecular weight like R600) because of a relatively larger turbine size. The relation between the RIT's performance (i.e. efficiency and output power) is shown in Fig. 6a,b, where the best RIT performance was seen at an expansion ratio of 3.0. For the total expansion ratio, both the isentropic efficiency of the turbine and the actual enthalpy drop through the turbine stage indicated a growing development, leading to the maximisation of the RIT's output power for whole the considered organic fluids. The

output power was seen to increase with increasing expansion ratio due to an actually large enthalpy drop across the RIT stage through the expansion process.

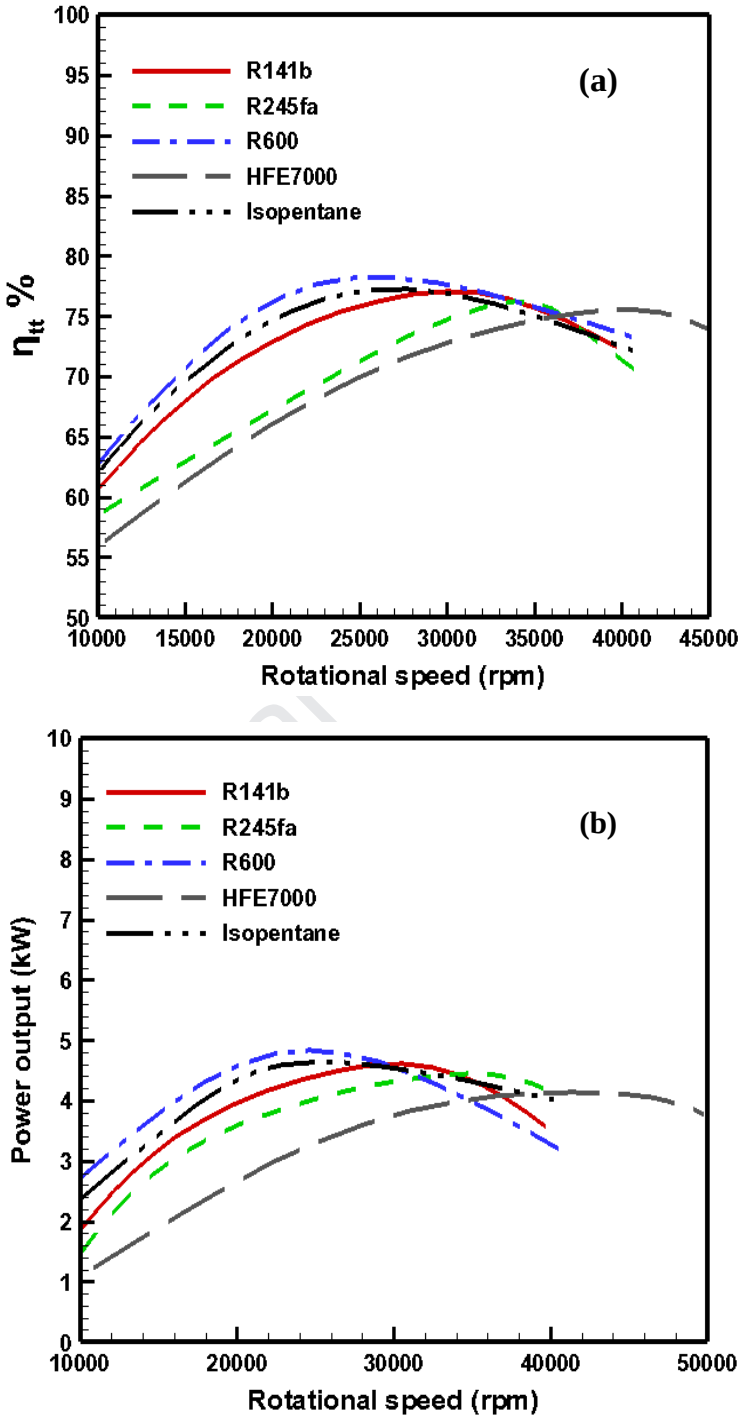

Fig. 5 Influence of the rotational speed on the RIT efficiency (a), and power (b), for five organic fluids

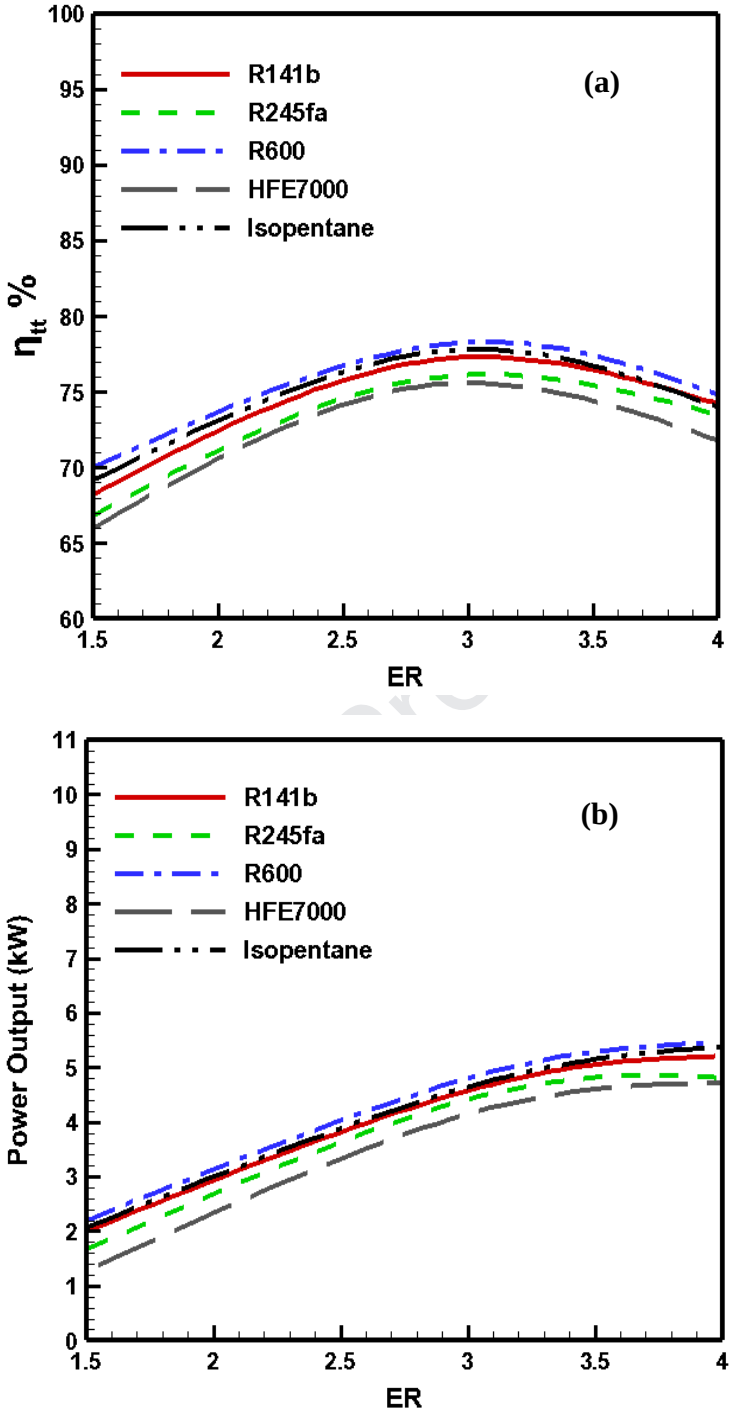

Fig. 6 Impact of the expansion ration on the RIT efficiency (a), and power (b), for five organic fluids

Fig. 7 illustrates the velocity vector through the stage of the RIT turbine, which demonstrates the vortex formation and flow circulation at the rotor blades leading edge of the RIT. A slight flow separation along with secondary flow on the suction-side surface (SS) just down-stream of the leading-edge and flow was seen to develop smoothly, as

281 presented after this section. Due to the low-velocity level of the working fluid, the viscous shear force became
282 dominate through the flow passages of the rotor leading to a high level of entropy generation. Therefore,
283 improvement of the blade's profile of the rotor (i.e. the blade thickness distribution and the blade angles) is required.
284 A high velocity occurs at stator exit due to high expansion ratios in small-scale which leads to a higher friction loss.
285 High flow velocity is expected because of the sudden expansion of the flow through the throat area of the stator.
286 Moreover, the opening of the throat area has an effect on the flow velocity where the working fluid is accelerated by
287 the pressure drop. The pressure loss through the stator passages is considerably high and yields the shock waves. In
288 small-scale ORC turbines, the flow recirculation is remarked because of the high loading on the blades. Where the
289 flow separation always happens on the suction side of the blades because of the high loading which deaccelerates
290 the working fluid relative velocity.

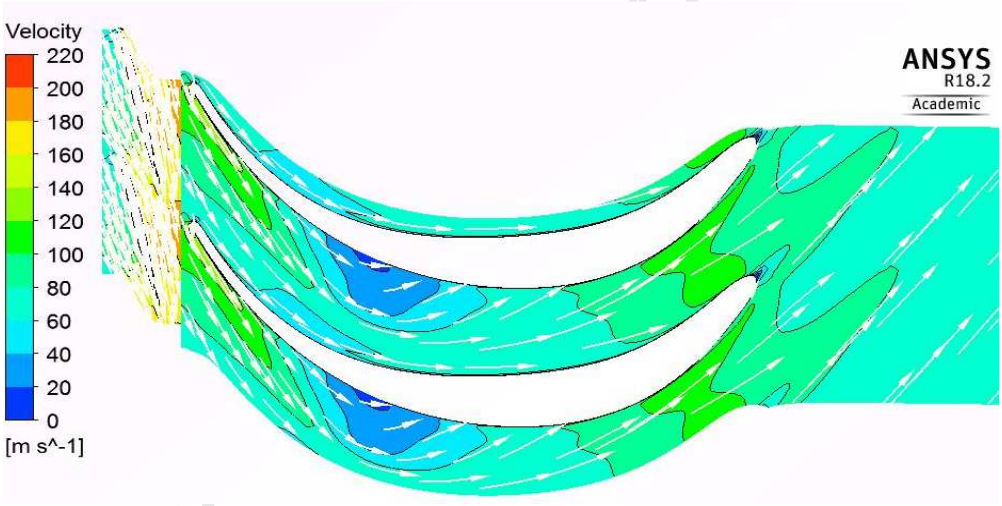

Fig. 7 Velocity vector at mid-span of the rotor blades with working fluid R245fa

291

292 **4.2. Off-design results**

293 In the off-design simulations, the rotational speeds were varied from 0.8 to 1.2 of the design speed of 350000 rpm.
294 While the expansion ratios were changed from 1.75 to 4.0 at the design expansion ratio of 3.0. Furthermore, the
295 turbine inlet temperatures were changed from 345 K to 385 K with R245fa as a working fluid.
296 Fig. 8 presents the evolution of the RIT performance in terms of isentropic efficiency with turbine inlet temperature
297 and rotational speed, respectively; it shows the turbine efficiency can effectively be controlled by the turbine inlet
298 temperature at a nominal rotational speed. The maximum RIT isentropic efficiency is reached at rotational speed
299 ratio of 1.0 as a design point.

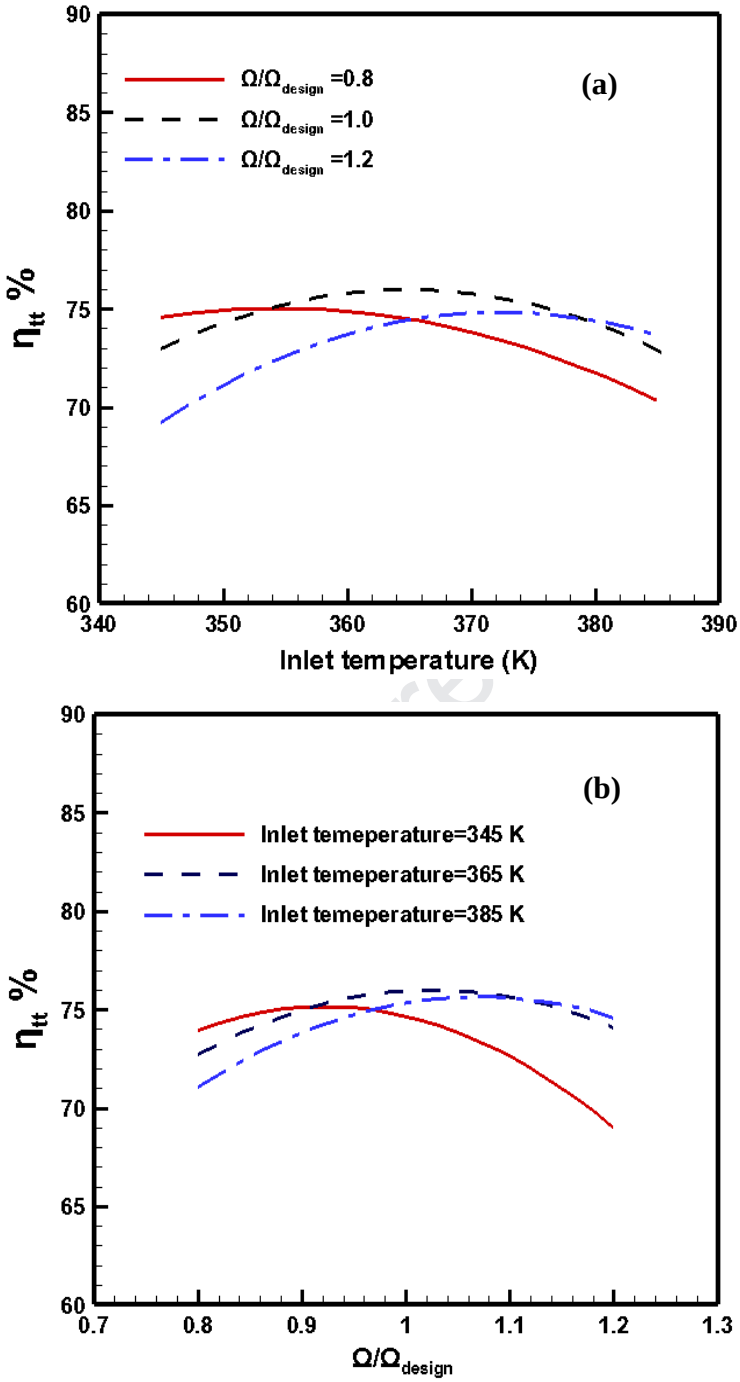

Fig. 8 The change of turbine efficiency with different inlet temperatures (a), and with rotational speeds (b), for the working fluid R245fa

Fig. 9a,b indicates the variation of the RIT power output with inlet turbine temperatures and rotational speed ratios at a mass flow rate of 0.25 kg/s. It can be noted from Fig. 9a that at different rotational speed ratios, the RIT power output increases with the inlet turbine temperature; the increase is more obvious at the highest ratio of the rotational

304 speed. In Fig. 9b, it can be observed that the maximum power output is at the highest rotational speed ratio.
305 Moreover, the turbine power output increases with inlet temperature at a constant rotational speed ratio.

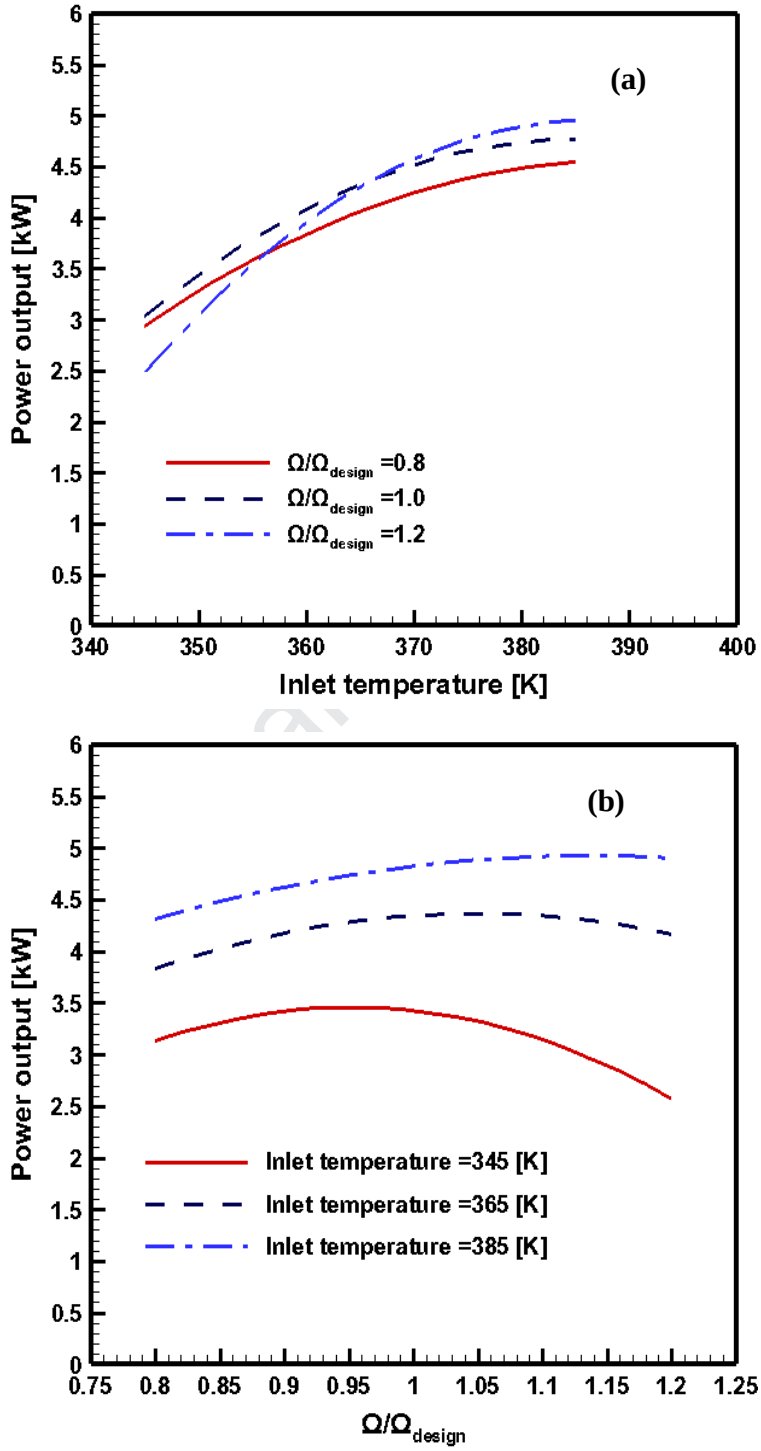

Fig. 9 Evolution of the RIT power output with inlet temperatures (a), and rotational speeds (b)
306

4.3. Validation of the PD design and CFD model against experimental results

Because of the limited heat source in our lab at the University of Birmingham, the experimental tests of the ORC system have been carried out at the mass flow rate of the working fluid (R245fa) of 0.09 kg/s. Consequently, the RIT was run at various off-design conditions comprising: expansion ratio, inlet pressure, inlet temperature, and rotational speed. Where three-dimensional CFD investigations of the RIT were conducted at similar off-design points, including a mass flow rate of 0.09 kg/s, a rotational speed from 7,500 rpm to 19,000 rpm, an expansion ratio from 1.25 to 2.2 and inlet temperatures ranging between 60°C - 75°C. Then, the comparison between the results gotten from the CFD model and experimental investigations in terms of the RIT global performance was performed.

In order to evaluate the overall performance small-scale ORC based on the developed RIT, and to validate the developed PD methodology based on 1D modelling and 3D CFD simulations, the experimental work was carried out at off-design points. Fig. 10a,b shows the comparison of the RIT performance between the developed PD methodology and CFD model with experimental results in terms of efficiency (a) and power (b) respectively. Where the performance bars were plotted as a function of expansion ratio at different off-design points. As shown in Fig. 10a,b, there is a marked difference between the obtained performance from the PD and CFD models. This deviation is due to the empirical correlations utilized in losses calculations through the PD stage which is underestimated the losses. However, the comparisons of the RIT efficiency and power with the expansion ratio for R245fa as a working fluid showed that the maximum deviations were 15.73% at off-design points. More details about the deviation are justified in the next paragraphs.

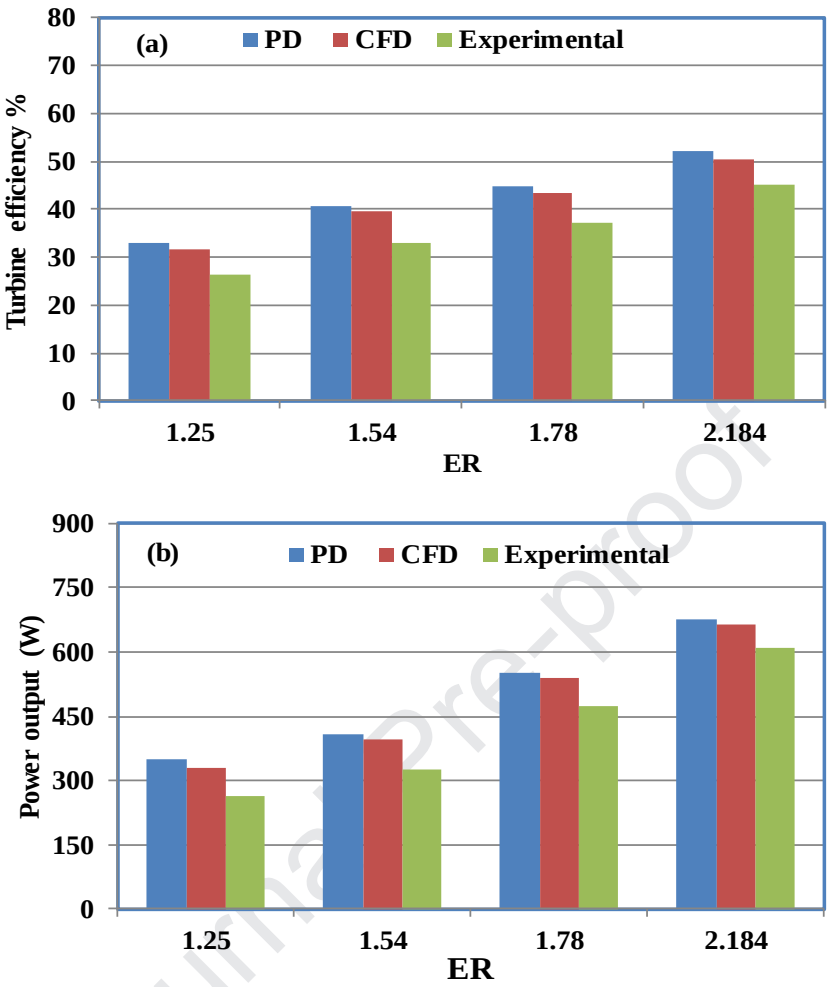

Fig. 10 Comparison of the RIT efficiency and power from the PD and CFD simulations with the experimental work in terms of turbine efficiency (a) and turbine power (b)

Fig. 11 compares the RIT efficiency and power delivered from the CFD simulations with experimental tests for various expansion ratios at an inlet temperature of 75°C. The change in the RIT performance with the inlet temperatures is shown in Fig. 12 at an expansion ratio of 2.2.

From the RIT global performance comparisons in Fig. 11 and Fig. 12, it is obvious that the RIT efficiency and power showed good consensus with the obtained results from the CFD investigations and experimental tests. The power and efficiency of the RIT increased when increasing expansion ratios and rotational speeds due to the rise in the specific actual enthalpy drop of the working fluid through the RIT stage. Furthermore, the rise in the working fluid inlet temperature produced a considerable rise in RIT power and efficiency. The experimental tests indicated that the maximum delivered RIT power and efficiency were found to be 625.123 W and 45.22%, respectively. Fig.

11 and Fig. 12 exhibit that the delivered RIT power and efficiency i.e. global performance from the experimental tests were lower than the CFD results.

The variances between the experimental tests and CFD simulations can be attributed because of the assumption of the smooth blade wall that was used in the CFD model, compared with the roughness of the manufactured blade surface. Moreover, the actual experimental tests were associated with slightly transitional behaviour; while the steady-state condition was applied in the CFD simulations. Also, the vibration and the mechanical loss in terms of friction losses because of the coupling of the rotor shaft with the bearing, torque meter, and shaft seal, can be attributed to the decrease in the RIT performance (i.e. power and efficiency); which was delivered from the experimental test related to the CFD simulations. Depending on these experimental results at off-design conditions, the offered design methodology of the turbine can be employed to evaluate the flow characteristics and the turbine performance.

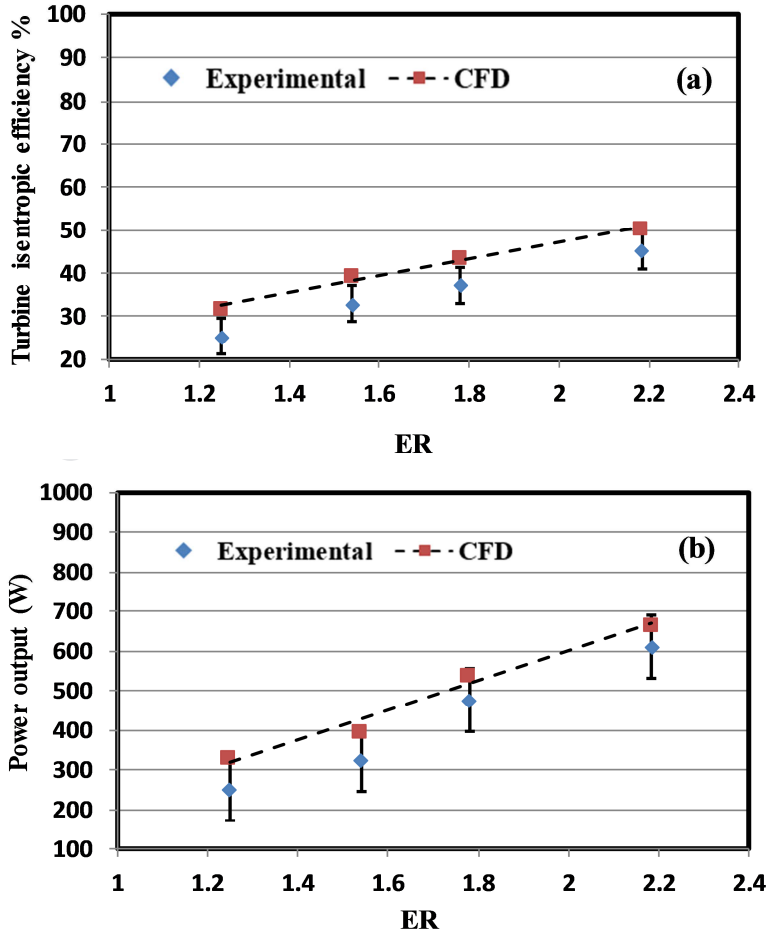

Fig. 11 Comparison between the results from the CFD simulation and experimental tests of RIT efficiency (a), and power output (b)

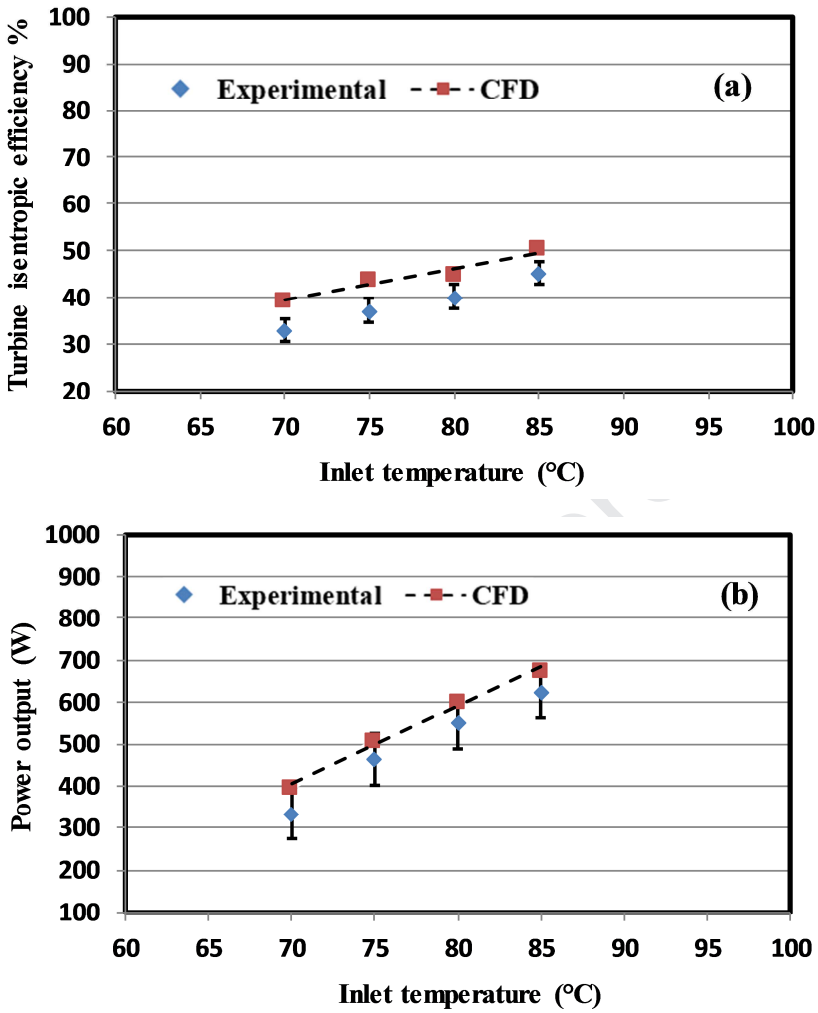

Fig. 12 Comparison between the results from the CFD simulation and experimental tests of RIT efficiency (a), and power (b), with inlet temperature

To evaluate the ORC system's thermal efficiency with the R245fa as a working fluid, the performance of the RIT turbine was fed into the thermodynamic cycle analysis model. Where, the relationship between the RIT turbine efficiency, the ORC system efficiency and heat sink temperature (i.e. cooling medium/water) was presented in Fig. 13. It is clear from Fig. 13 that the RIT efficiency is fairly constant with increasing the heat sink temperature. At high heat sink temperature, the difference between the evaporator temperature and condenser temperature is low. Also, it can be concluded that the ORC system efficiency was very sensitive to heat sink temperature.

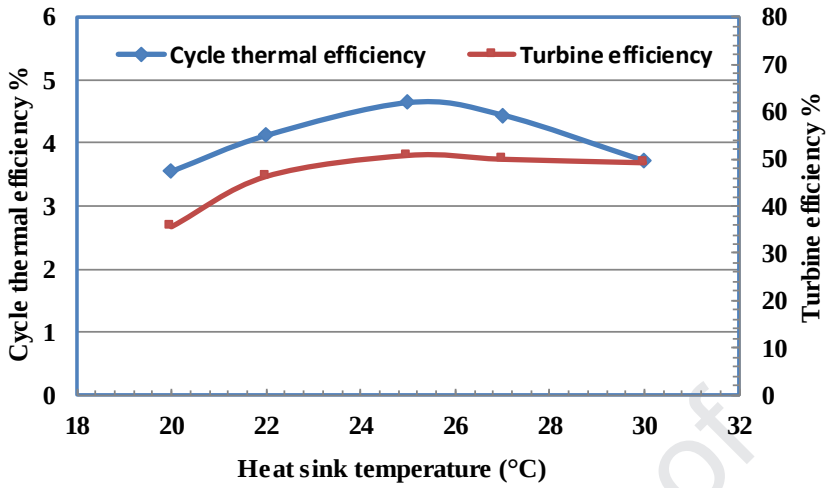

Fig. 13 Variation of ORC cycle and RIT efficiencies with heat sink temperature for R245fa

The obtained ORC system thermal efficiency from the experimental tests using the R245fa as a working fluid is compared with the published literature (Abadi et al., 2015; Jung et al., 2015; Li et al., 2015; Wang et al., 2010; Xi et al., 2017) on the ORC system using different zeotropic mixtures as working fluids as shown in Fig. 14. It can be noticed that the ORC system at off-design points with R245fa as a working fluid achieved considerably higher system thermal efficiency compared with other studies. It is probable to reach a maximum system thermal efficiency of 4.25% with the current work. To highlight the possibility of the offered combined methodology (small-scale ORC-RIT model), the comparison was carried out with the results of other published researches that used some mixture fluids. In the current study, R245fa was used as a working fluid. Greater ORC system thermal efficiency from mixture fluid can be achieved compared with R245fa when considering the environmental factors in the analysis.

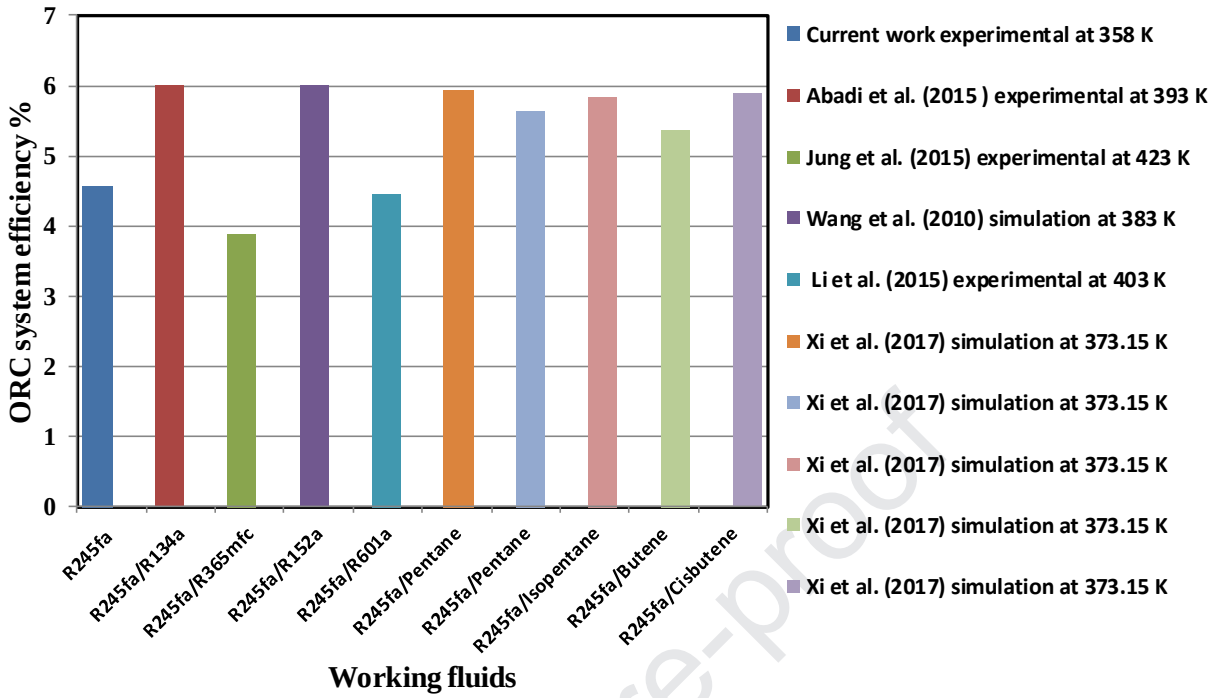

Fig. 14 Comparison of the obtained ORC system thermal efficiency from the current study with other studies for various mixture fluids

5. Conclusions

The current work aimed to develop a new systematic prediction methodology of a small-scale ORC RIT performance based on the preliminary design PD, 3D CFD analyses, system thermodynamics analysis, and experimental tests. The development PD methodology involved a genetic algorithm optimization technique that is integrated with the PD model to assess the influence of the design input parameters on the turbine performance and geometry. Due to the complex flow nature through the RIT stage, the 3D CFD simulations using ANSYS-CFX was employed to evaluate the turbine performance and to investigate the flow characteristics at design and off-design operating points. Five different working fluids (R141b, R245fa, R600, HFE7000 and isopentane) were investigated through PD modelling and CFD analysis. Moreover, the designed RIT turbine was manufactured based on the new 3D printing technique (additive layer manufacturing).

The parametric analyses were carried out to assess the effects of varying system parameters and operating conditions on the system performance. Therefore, the CFD analysis can properly and accurately examine the RIT performance under design and off-design conditions with various organic fluids. The high-density working fluids lead to new unconventional blade geometry and configuration. Where backswept blading leads to an increase in turbine

performance. From the 3D CFD simulation results under all design conditions, R600 as the working fluid was found to exhibit the highest RIT performance, where the maximum power output and isentropic efficiency was 4.8 kW and 78.32%, respectively. The ORC performance is considerably affected by the RIT isentropic efficiency and output power; thus, to achieve an efficient ORC system, there is a need for a high RIT performance. The experimental results at off-design points showed that the maximum ORC efficiency was around 4.25%. The obtained results from the ORC experimental test facility under off-design conditions with R245fa illustrated that the ORC and RIT efficiencies depend on rotational speed, inlet temperature, and expansion ratio. In small scale RIT at high rotational speeds, the vibration can be another parameter should be included in both the PD design and CFD model. Moreover, the transient CFD model is required to consider the effect of nozzle-rotor interactions on RIT performance in future work.

Declaration

The authors declare no competing financial interest.

Appendix A. Supplementary material

References

ANSYS CFX-Solver Modelling Guide. Release 18.2, 2017.

Abadi, G.B., Yun, E., Kim, K.C., 2015. Experimental study of a 1 kw organic Rankine cycle with a zeotropic mixture of R245fa/R134a. Energy 93, 2363-2373.

Al Jubori, A., Al-Dadah, R.K., Mahmoud S., Khalil, K.M., Bahr Ennil, A.S., 2016. Development of efficient small scale axial turbine for solar driven organic Rankine cycle. Proceedings of ASME Turbo Expo 2016, Seoul, South Korea, paper no GT2016-57845, V003T25A011-22. https://doi.org/10.1115/GT2016-57845

Al Jubori, A.M., Al-Dadah, R., Mahmoud, S., 2017a. An innovative small-scale two-stage axial turbine for low-temperature organic Rankine cycle. Energy Conversion and Management 144, 18-33.

Al Jubori, A.M., Al-Dadah, R., Mahmoud, S., 2017b. New performance maps for selecting suitable small-scale turbine configuration for low-power organic Rankine cycle applications. Journal of cleaner production. 161, 931-946.

Alshammari, F., Pesyridis, A., Karvountzis-Kontakiotis, A., Franchetti, B., Pesmazoglou, Y., 2018. Experimental study of a small scale organic Rankine cycle waste heat recovery system for a heavy duty diesel engine with focus on the radial inflow turbine expander performance. Applied energy 215, 543-555.

Chen, F., Liu, L., Peng, J., Ge, Y., Wu, H., Liu, W., 2019. Theoretical and experimental research on the thermal performance of ocean thermal energy conversion system using the rankine cycle mode. Energy 83,497-503.

Cho, S.-Y., Cho, C.-H., Ahn, K.-Y., Lee, Y.D., 2014. A study of the optimal operating conditions in the organic Rankine cycle using a turbo-expander for fluctuations of the available thermal energy. Energy 64, 900-911.

Costall, A., Hernandez, A.G., Newton, P., Martinez-Botas, R., 2015. Design methodology for radial turbo expanders in mobile organic Rankine cycle applications. Applied Energy 157, 729-743.

Glassman, A.J., 1995. Enhanced analysis and user's manual for radial-inflow turbine conceptual design code RTD. NASA CR 195454.

Jung, H.-C., Taylor, L., Krumdieck, S., 2015. An experimental and modelling study of a 1 kW organic Rankine cycle unit with mixture working fluid. Energy 81, 601-614.

Kang, S.H., 2016. Design and preliminary tests of ORC (organic Rankine cycle) with two-stage radial turbine. Energy 96, 142-154.

Kim, D.-Y., Kim, Y.-T., 2017. Preliminary design and performance analysis of a radial inflow turbine for organic Rankine cycles. Applied Thermal Engineering 120, 549-559.
Klein, S.A., 2013. Engineering equation solver, F-chart Software. Middleton, WI.
Lemmon, E., Huber, M., McLinden, M., 2007. Reference fluid thermodynamic and transport properties–REFPROP Version 8.0. NIST standard reference database 23.
Li, T., Zhu, J., Fu, W., Hu, K., 2015. Experimental comparison of R245fa and R245fa/R601a for organic Rankine cycle using scroll expander. International Journal of Energy Research 39, 202-214.
Li, Y., Ren, X.-d., 2016. Investigation of the organic Rankine cycle (ORC) system and the radial-inflow turbine design. Applied Thermal Engineering 96, 547-554.
Lv, G., Yang, J., Shao, W., Wang, X., 2018. Aerodynamic design optimization of radial-inflow turbine in supercritical CO 2 cycles using a one-dimensional model. Energy Conversion and Management 165, 827-839.
Moustapha, H., Zelesky, M.F., Baines, N.C., Japikse, D., 2003. Axial and radial turbines. Concepts NREC White River Junction, VT.
Nithesh, K., Chatterjee, D., 2016. Numerical prediction of the performance of radial inflow turbine designed for ocean thermal energy conversion system. Applied Energy 167, 1-16.
Pei, G., Li, J., Li, Y., Wang, D., Ji, J., 2011. Construction and dynamic test of a small-scale organic rankine cycle. Energy 36, 3215-3223.
Russell, H., Rowlands, A., Ventura, C., Jahn, I., 2016. Design and testing process for a 7kw radial inflow refrigerant Turbine at the University of Queensland, ASME Turbo Expo 2016: Turbomachinery Technical Conference and Exposition. American Society of Mechanical Engineers, pp. V008T023A036-V008T023A036.
Shao, L., Zhu, J., Meng, X., Wei, X., Ma, X., 2017. Experimental study of an organic Rankine cycle system with radial inflow turbine and R123. Applied Thermal Engineering 124, 940-947.
Stijepovic, M.Z., Papadopoulos, A.I., Linke, P., Stijepovic, V., Grujic, A.S., Kijevčanin, M., Seferlis, P., 2017. Organic Rankine Cycle system performance targeting and design for multiple heat sources with simultaneous working fluid selection. Journal of cleaner production 142, 1950-1970.
Sung, T., Yun, E., Kim, H.D., Yoon, S.Y., Choi, B.S., Kim, K., Kim, J., Jung, Y.B., Kim, K.C., 2016. Performance characteristics of a 200-kW organic Rankine cycle system in a steel processing plant. Applied Energy 183, 623-635.
Ventura, C.A., Jacobs, P.A., Rowlands, A.S., Petrie-Repar, P., Sauret, E., 2012. Preliminary design and performance estimation of radial inflow turbines: An automated approach. Journal of Fluids Engineering 134, 031102.
Wang, J., Zhao, L., Wang, X., 2010. A comparative study of pure and zeotropic mixtures in low-temperature solar Rankine cycle. Applied Energy 87, 3366-3373.
Weiß, A.P., Popp, T., Müller, J., Hauer, J., Brüggemann, D., Preißinger, M., 2018. Experimental characterization and comparison of an axial and a cantilever micro-turbine for small-scale Organic Rankine Cycle. Applied Thermal Engineering 140, 235-244.
Whitfield, A., Baines, N.C., 1990. Design of radial turbomachines.
Xi, H., Li, M.-J., He, Y.-L., Zhang, Y.-W., 2017. Economical evaluation and optimization of organic Rankine cycle with mixture working fluids using R245fa as flame retardant. Applied Thermal Engineering 113, 1056-1070.
Xi, H., Li, M.-J., Zhang, H.-H., He, Y.-L., 2019. Experimental studies of organic Rankine cycle systems using scroll expanders with different suction volumes. Journal of Cleaner Production 218, 241-249.
Yang, J., Sun, Z., Yu, B., Chen, J., 2018. Experimental comparison and optimization guidance of R1233zd (E) as a drop-in replacement to R245fa for organic Rankine cycle application. Applied Thermal Engineering 141, 10-19.
Zheng, Y., Hu, D., Cao, Y., Dai, Y., 2017. Preliminary design and off-design performance analysis of an Organic Rankine Cycle radial-inflow turbine based on mathematic method and CFD method. Applied Thermal Engineering 112, 25-37.
Ziviani, D., James, N.A., Accorsi, F.A., Braun, J.E., Groll, E.A., 2018. Experimental and numerical analyses of a 5 kWe oil-free open-drive scroll expander for small-scale organic Rankine cycle (ORC) applications. Applied energy 230, 1140-1156.

Nomenclature

b	blade width (m)	***Subscript/superscript***	
C	flow absolute velocity (m/s)	1-5	station within the turbine and cycle
d	diameter (m)	cr	critical

f	friction coefficient (-)	e	evaporator
h	enthalpy (kJ/kg)	H	hot
l	length (m)	hyd	hydraulic
K	losses coefficients (-)	L	low
k	specific turbulence kinetic energy (m^2/s^2)	LE	leading edge
$\dot{m}$	mass flow rate (kg/s)	nbp	normal boiling point
p	pressure (bar)	r	radial
$\dot{Q}$	heat (kW)	t	turbine
r	radius (m)	TE	trailing edge
s	entropy (kJ/kg.K)	th	thermal
T	temperature (K)	tt	total-to-total
t	time (s)	x	axial
U	turbine blade velocity (m/s)	θ	tangential/circumferential direction
w	flow relative velocity (m/s)	***Acronyms***	
$\dot{W}$	power output (kW)	1D, 2D, 3D	one, two and three-dimensional
Z	number of blade (-)	CFD	computational fluid dynamics
		CAD	computer aided design
Greek symbols		GWP	global warming potential
α	absolute flow angle (degree)	ODP	ozone depletion potential
β	relative flow angle (degree)	ORC	organic Rankine cycle
η	efficiency (%)	PD	preliminary design
ρ	density (kg/m^3)	RIT	radial-inflow turbine
ε	clearance (m)	RANS	Reynolds-averaged Navier-Stokes
ψ	loading coefficient (-)	SST	shear stress transport
ϕ	flow coefficient (-)		
ω	specific turbulence dissipation rate (m^2/s^3)		

477

Highlights

- 1D design, 3D simulation and manufacturing of radial-inflow turbine are presented.
- Five working fluids (R141b, R245fa, R600, HFE7000, isopentane) are investigated.
- Efficiency characteristics of the turbine at design and off-design behaviour are conducted.
- The maximum turbine efficiency and power are 78.32% and 4.8 kW.
- Higher turbine and thermal system efficiencies achieved using working fluid R600.

Contribution section

All authors have made substantial contributions through the submitted manuscript that entitled "Design and manufacturing a small-scale radial-inflow turbine for clean organic Rankine" as following:

Conceptualization: Ayad M. Al Jubori

Methodology: Ayad M. Al Jubori and Kiyarash Rahbar

Software: Ayad M. Al Jubori and Kiyarash Rahbar

Formal analysis: Ayad M. Al Jubori and Fadhel N. Al-Mousawi

Acquisition of data: Ayad M. Al Jubori and Fadhel N. Al-Mousawi

Writing - Original Draft: Ayad M. Al Jubori

Writing - Review & Editing: Raya Al-Dadah and Saad Mahmoud

Visualization: Ayad M. Al Jubori and Saad Mahmoud

Critical revision: Raya Al-Dadah and Saad Mahmoud